

PROBE COMPENSATION CHARACTERIZATION AND ERROR ANALYSIS IN CYLINDRICAL NEAR-FIELD SCANNING

Ziad A. Hussein

Jet Propulsion Laboratory
California Institute of Technology
Pasadena, California 91109

ABSTRACT

A novel computer simulation methodology to properly characterize the role of probe directivity/pattern compensation in cylindrical near-field scanning geometry is presented. The methodology is applied to a linear test array antenna and the JPL/NASA scatterometer (NSCAT) radar antenna. In addition, error analysis techniques of computer simulation and measured tests, have been developed to determine the achievable accuracy in pattern measurements of the NSCAT antenna in cylindrical near field.

Keywords: Near-field measurements, cylindrical scanning, probe compensation, near-field errors.

1. INTRODUCTION

The recent evolution of spaceborne scatterometers is demanding very high quality performance from antennas. For example, a recently designed JPL/NASA spaceborne scatterometer for global mapping of dynamic change of ocean circulation requires accurate knowledge of wide-angle antenna patterns, squint angle, and beamwidth. The antennas assembled on this instrument are each a ku-band 3-m long stick slotted waveguide type.

Near-field measurement has been used for many years to determine the far-field radiation patterns of antennas with high accuracy [1]. In order to accurately characterize the radiation performance of NSCAT at JPL, a cylindrical near-field measurement facility has been developed (Figure 1). It is the objective of this paper to present a methodology to properly characterize the role of probe-pattern compensation in cylindrical near field [2] and to critically assess the importance of different error mechanisms in evaluating the achievable accuracy in pattern measurements. Probe characterization and pattern assessment have been performed both by utilizing a novel simulation algorithm and also by

using actual measured data. The novelty of this work is explained next.

2. PROBE COMPENSATION ANALYSIS

Consider an idealized circular-aperture probe that is modeled by its equivalent tangential electric currents, J_s , in the $x_p = 0$ plane of the probe-coordinate system shown in Figure 2. The currents on the circular-aperture plane can be written as

$$\begin{aligned}\vec{J}_s &= \hat{x}_p \times \vec{H}_p \\ \vec{M}_s &= -\hat{x}_p \times \vec{E}_p = 0\end{aligned}\quad (1)$$

Interaction between the probe equivalent aperture currents and the test antenna fields (\vec{E}_a, \vec{H}_a) can be obtained with the application of reciprocity theorem to yield to the probe vector output, neglecting multiple scattering between the probe and antenna under test (AUT)

$$P^{(1,2)} = \int_{S_p} (\vec{M}_s \cdot \vec{H}_a - \vec{J}_s \cdot \vec{E}_a) dS \quad (2)$$

In equation (2), superscripts (1,2) designate two orientations of the probe necessary to construct the far-field pattern of the test antenna. Specifically, P^1 and P^2 correspond to the probe response for the electric current, J_s , oriented in the z_p and $-y_p$ direction respectively. Assuming a uniform current across the probe, the integral in equation (2) is then approximated by

$$\begin{aligned}P^1 &\approx \int_{S_p} E_z(\rho, \phi, z) \rho_p d\phi_p d\rho_p \\ P^2 &\approx \int_{S_p} E_\phi(\rho, \phi, z) \rho_p d\phi_p d\rho_p\end{aligned}\quad (3)$$

where (ρ_p, ϕ_p) defines the polar coordinate in the aperture of the probe S_p , and E_z, E_ϕ are the fields in the cylindrical-coordinate system of the test antenna computed on the probe aperture. The use of an idealized circular-aperture probe with different radii, permits us to derive a closed form expression for its far-field radiation pattern. For a uniform magnetic field, H_p , in the aperture of the probe oriented in the y_p direction, the probe pattern is given by

$$\begin{aligned}\vec{E}_{\theta p}^1 &= \sin \theta_p \frac{J_1(u)}{u} \hat{\theta}_p \\ \vec{E}_{\phi p}^1 &= 0 \hat{\phi}_p\end{aligned}\quad (4)$$

and for a 90° rotation of the probe, it yields

$$\begin{aligned}\vec{E}_{\theta p}^2 &= \cos \theta_p \sin \phi_p \frac{J_1(u)}{u} \hat{\theta}_p \\ \vec{E}_{\phi p}^2 &= \cos \phi_p \frac{J_1(u)}{u} \hat{\phi}_p\end{aligned}\quad (5)$$

where $u = k a \sin(\alpha)$, $\cos(\alpha) = \sin(\theta_p) \cos(\phi_p)$, a is the probe radius, k is the wavenumber $2\pi/\lambda$, and $J_1(u)$ is the Bessel function of the first kind. To perform probe-pattern compensation, one needs the cylindrical wave expansion of the probe fields from the following expressions (assuming no fields in the back of the probe) [2]:

$$\begin{aligned}a_m^2(k \cos \theta_p) &= \frac{1}{j^m \sin \theta_p} \int_{-\pi/2}^{\pi/2} E_{\phi p}^2(\theta_p, \phi_p) e^{-jm \phi_p} d\phi_p \\ b_m^2(k \cos \theta_p) &= \frac{1}{j^{m+1} \sin \theta_p} \int_{-\pi/2}^{\pi/2} E_{\theta p}^2(\theta_p, \phi_p) e^{-jm \phi_p} d\phi_p\end{aligned}\quad (6)$$

where $m < ka$. Similarly, one could obtain the probe coefficients, a_m^1 and b_m^1 , for the other field components, $E_{\theta p}^1$ and $E_{\phi p}^1$. These results, together with the probe vector output response (equations 3-6 are numerical) and evaluated) allow us to perform computer-simulated synthetic measurements and provide accurate insight unattainable or costly in measurement alone. The test antenna fields, E_θ and E_ϕ , are then constructed in terms of the probe vector output response and probe antenna coefficients

derived from application of the reciprocity theorem [3-4]

$$\begin{aligned}\vec{E}_\phi(\theta, \phi) &= \sin \theta \sum_{|n| < kr} j^n a_n(k \cos \theta) e^{jn \phi} \hat{\phi} \\ \vec{E}_\theta(\theta, \phi) &= \sin \theta \sum_{|n| < kr} j^{n+1} b_n(k \cos \theta) e^{jn \phi} \hat{\theta}\end{aligned}\quad (7)$$

where r is the smallest radius enclosing the test antenna and a_n, b_n are the cylindrical wave coefficients of the test antenna given by

$$a_n(k \cos \theta) = \frac{T_n^1(k \cos \theta) \alpha_m^2(k \cos \theta) T_n^2(k \cos \theta) \alpha_m^1(k \cos \theta)}{\sin^2 \theta \Delta_n(k \cos \theta)}\quad (8)$$

$$b_n(k \cos \theta) = \frac{T_n^2(k \cos \theta) \gamma_m^1(k \cos \theta) - T_n^1(k \cos \theta) \gamma_m^2(k \cos \theta)}{\sin^2 \theta \Delta_n(k \cos \theta)}\quad (9)$$

$$T_n^{(1,2)}(k \cos \theta) = \int_{-\infty-\pi}^{\infty} \int_{-\pi}^{\pi} P^{(1,2)} e^{-jn \phi} e^{jk \cos \theta z} d\phi dz\quad (10)$$

$$\Delta_n(k \cos \theta) = \gamma_m^1(k \cos \theta) \alpha_m^2(k \cos \theta) - \gamma_m^2(k \cos \theta) \alpha_m^1(k \cos \theta)\quad (11)$$

$$\begin{aligned}\alpha_m^{(1,2)}(k \cos \theta) &= \sum_{|m| < ka} b_m^{(1,2)}(k \cos \theta_p) H_{n+m}^2(k r_0 \sin \theta) \\ \gamma_m^{(1,2)}(k \cos \theta) &= \sum_{|m| < ka} a_m^{(1,2)}(k \cos \theta_p) H_{n+m}^2(k r_0 \sin \theta)\end{aligned}\quad (12)$$

and where H_{n+m}^2 is the Hankel function of the second kind and r_0 is the sampling cylinder radius. In the limit as the probe radius becomes very small, the probe output of equation 3 is the direct response of the near field at a point, that is the response of

infinitesimal hertzian dipole, $P^1=E_z$ and $P^2=E_\phi$, and no probe compensation is needed. Also, note from equation 6 and Figure 2 that probe compensation at observation angle θ necessitates the knowledge of the probe fields in the azimuthal direction at observation angle $\theta_p=\pi-\theta$. Consequently, the calculation of the principal elevation plane of the test antenna, for example, requires 3D probe fm-field patterns.

Next, simulation examples are given to determine the role of low- and high-directivity probes in the implementation of a probe-pattern compensation technique. Two different test antenna examples are considered: 15-element linear array and the JPL/NASA scatterometer slotted-waveguide radar antenna.

3. 15-Element Test Array Results

In this example, a 15-element infinitesimal dipole array is located along the z-axis with interelement spacing of a half wavelength. Each element is fed with unit amplitude and zero phase. The idealized circular aperture probe vector output integral equation (3) is then evaluated for each probe position on the required sampling point on a cylindrical near-field surface enclosing the test antenna.

Figure 3 shows the simulated near-field results along the z-axis at $r_0=4\lambda$. Three different probe radii are used in this simulation, namely 0.3λ , 0.5λ , and 1λ , which correspond to probe directivities of 5.5dB, 9.94dB and 15.96dB respectively. Figure 4 depicts the corresponding probe far-field patterns at $\phi_p=0$ degrees. To illustrate the effect of probe directivity, the test antenna far-field patterns are calculated for each probe size with and without probe pattern compensation and compared to the exact solution results, as shown in Figures 5, 6 and 7.

In this investigation, Figure 7 shows that probe compensation at probe pattern null is possible when near-field simulated measurement is carried out at $r_0=4\lambda$. Near fields for a 15-element array antenna similar to Figure 3 are computed at $r_0=8\lambda$. It is observed a small distortion on the compensated pattern at the observation angle that corresponds to probe pattern null. The prevailing use of high-directivity probes in cylindrical near-field may be dependent on the sampling radius r_0 . Furthermore, a probe with low directivity, e.g. 5.5dB, needs a little probe correction if any near the test antenna main beam, as shown in Figure 5.

4. JPL/NASA Scatterometer Antenna Results

Since the 15-element linear array antenna has an omnidirectional pattern in the azimuthal direction, it is difficult to obtain an insight into the effect of pattern compensation in that direction. As an alternative, simulations of the 6-dB pedestal near-fields tapered illumination of the JPL/NASA slotted waveguide array antenna (Figure 8) are implemented using the circular-aperture probe with an arbitrary radius. The antenna is 3.06m long and 6.3cm wide operating at Ku-band (13.995 GHz); Antenna directivity is approximately 34dB.

In the first simulation example, a probe radius of $a=.5\lambda$ at $r_0=5\lambda$ is utilized. Far-field patterns, with and without probe pattern compensation, are calculated and compared to the exact solution in the azimuth direction. The results were compared and are given in Figure 9. One observation is that the need for probe compensation is more pronounced at an angle close to the main beam peak. However, the use of a low-directivity probe, $a=.3\lambda$, at the radial distance $r_0=5\lambda$ results in less crucial probe-pattern compensation in the same direction. In general, computer-simulated synthetic measurements with different idealized circular-aperture probes show similar observations in elevation as those presented for the 15-element linear array. A cylindrical near-field measurement of the JPL/NASA antenna with dual orthomode probe (9.57dB gain port 1 and 9.65dB port 2) supported these observations [5].

5. ERROR ANALYSIS

Error-analysis techniques are often employed in conjunction with near-field measurements to determine a reliable estimate of errors in the computed far field [6]. Among the near-field scanning geometries - planar, cylindrical and spherical- cylindrical near-field scanning is found to be the most suitable to calibrate JPL/NASA scatterometer antennas because it possesses a wide beam in the azimuth direction. Calibration requires accuracy in relative gain of 0.25 dB over ± 40 degree in the azimuth direction (wide beam), antenna-pointing accuracy of 0.05 degrees, and a narrow 3-dB beamwidth of 0.015 degrees. In this work, a novel computer simulation and measurement tests are employed when appropriate in the antenna calibration.

The accuracy of cylindrical near-field to far-field

transformation is influenced by various errors, which consist mainly of area truncation, probe positioning and orientation errors, AUT alignment, probe relative pattern, probe antenna interaction, receiver nonlinearity, and drift. The cylindrical near-field range facility at JPL, shown in Figure 1, is implemented such that the probe step along the tower (3.8m long) in the z-direction and the AUT rotates in azimuth. The insertion loss method [1] is adopted to obtain antenna gain. Hence, some additional systematic and random sources of errors can corrupt the calculated far-field pattern. These are mainly the AUT positioner rotary joint, attenuator and connectors used in the insertion loss measurement procedures. Analysis of some of these errors has already been performed [5-7].

Probe tower alignment is critical to antenna-pointing accuracy. Misalignment causes a pattern shift that is proportional to the slope of the tower. For example, it has been demonstrated with computer simulation that a 0.02-degree pointing error in elevation necessitates a probe-position alignment to better 1/16 wavelength. Multiple reflections between the probe and the antennas will greatly affect antenna gain and relative pattern accuracy [5]. Figure 10 shows deviations in far-field patterns computed from near-field data measured on successive cylindrical near-field surfaces separated by $\lambda/4$. Near-field truncation along the Z-direction will greatly affect the sidelobe level and periodicity in the elevation plane. Figure 11 illustrates the effect on the antenna peak gain for different scan lengths. A near-field truncation error in the azimuthal direction will deter our ability to predict the backlobe far-field patterns in that direction. It is seen from Figure 12 that the pattern deteriorates rapidly in azimuth, starting at an angle coinciding with the truncated angular near-field region. Accurate determination of the radial separation distance, r_0 , between the AUT and the phase center of the probe is important to predict antenna gain and relative patterns. Figure 13 describes the relative change of antenna gain vs. radial error.

REFERENCES

- [1] Special Issue on Near-Field Scanning Techniques, *IEEE Trans.*, Antennas and Propagat., Vol. AP-36, June 1988.
- [2] Z.A. Hussein and Y. Rahmat-Samii, "Probe Compensation Characterization in Cylindrical Near-

Field Scanning" *IEEE A P-S Symp. Digest*, Ann Arbor, Michigan, June 1993.

[3] A.D. Yaghjian, "Near-Field Antenna Measurement On A Cylindrical Surface: A Source Scattering-Matrix Formulation", *NBS Tech. Note* 696, July 1977.

[4] W.M. Leach Jr. and D.T. Paris, "Probe Compensated Near-Field Measurements On A Cylinder" *IEEE Trans*, vol. AP-21, No 4, pp. 435-445, July 1973,

[5] Z.A. Hussein, "NASA Scatterometer cylindrical Near-Field Error Analysis and Calibration *JPL, Interoffice Memorandum* 3361-94-094, Dec. 2, 1993.

[6] A.C. Newell, "Error Analysis Technique for Planar Near-Field Measurements" *IEEE Trans., Antenna and Propagat.*, Vol. AP-36, pp. 754-768, June 1988

[7] Z.A. Hussein, " NASA Scatterometer RF Calibration for Flight and Spare Antennas: Near-Field Data Processing and Analysis Final Report" *JPL Interoffice Memorandum* 336-94-095, May 16, 1994.

ACKNOWLEDGEMENT

This work was carried out at the Jet Propulsion Laboratory, under contract with the National Aeronautics and Space Administration. The author would like to thank K. Kellogg, R. Grabarsky, R. Thomas and Dr. C. Stubenrauch for their discussions and assistance in the measurement for the error analysis.

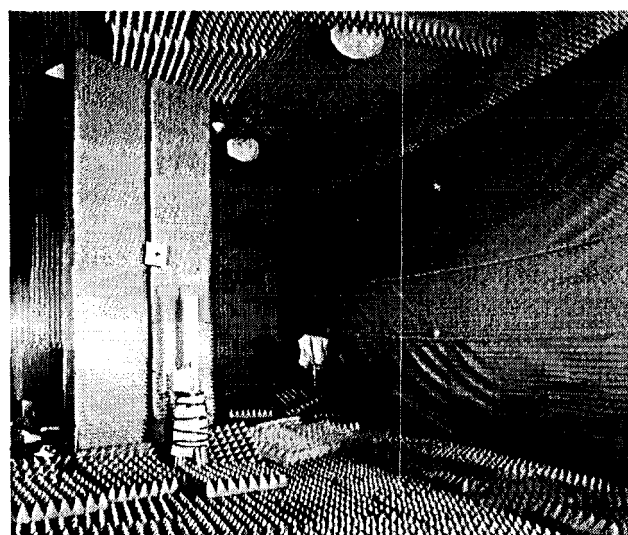


Figure 1. Cylindrical near-field measurement facility at JPL.

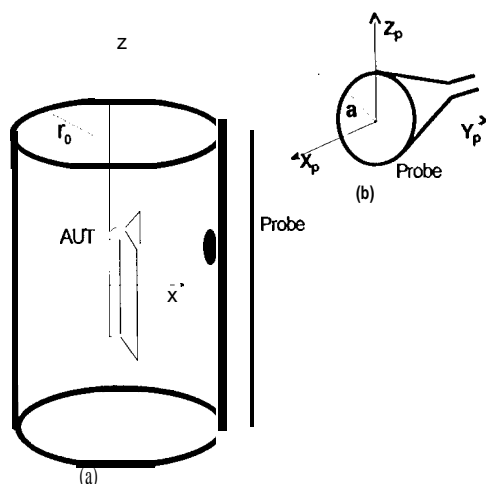


Figure 2. (a) Cylindrical near-field configuration and (b) probe coordinate system,

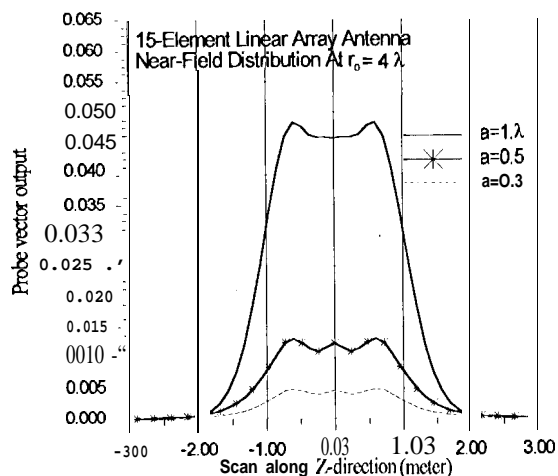


Figure 3. Near-field simulated probe response with different probe radii a , vs. scan angle along the z -direction.

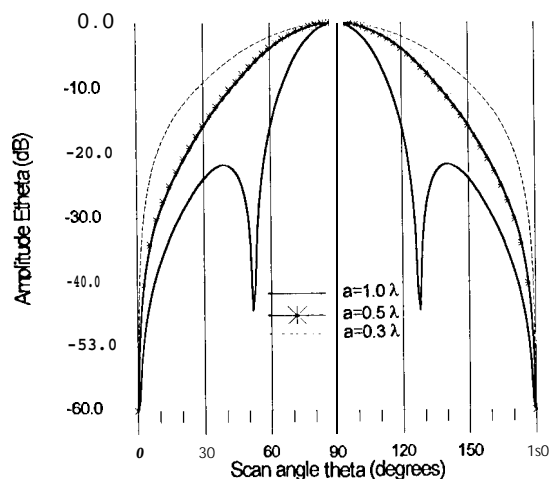


Figure 4. Far-field patterns of an idealized circular-aperture probe with different radii,

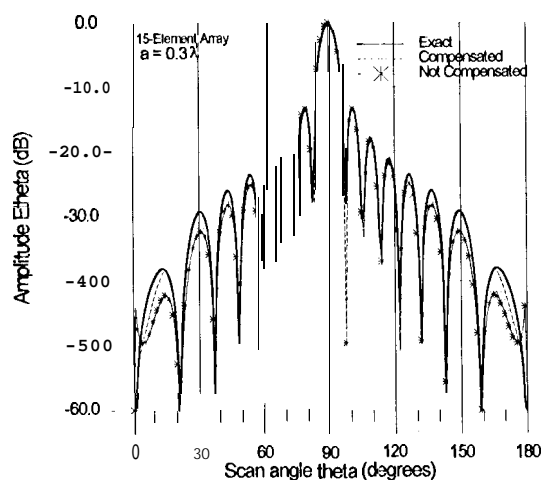


Figure 5. Comparison of exact solution and far-fields obtained from simulated near-field data with a probe radius $a = 0.3 \lambda$.

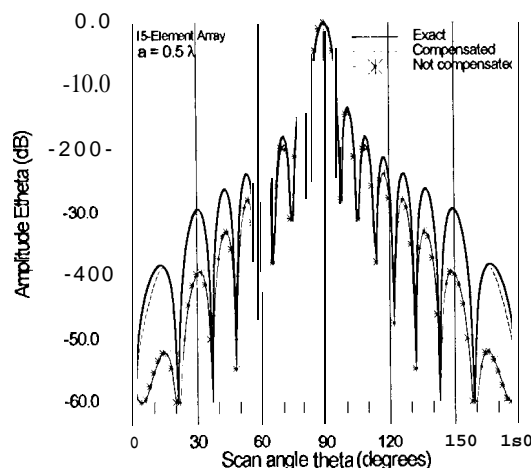


Figure 6. Comparison of exact solution and far-fields obtained from simulated near-field data with a probe radius $a = 0.5 \lambda$.

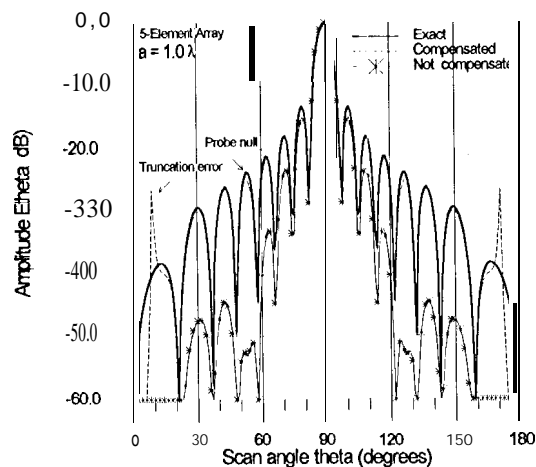


Figure 7. Comparison of exact solution and far-fields obtained from simulated near field data with a probe radius $a = 1.0 \lambda$.

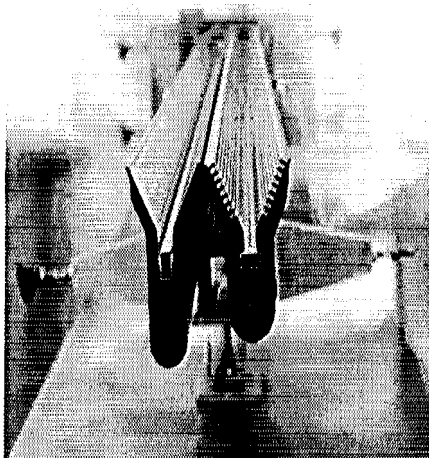


Figure 8. JPL/NASA antenna prepared for cylindrical near-field measurement.

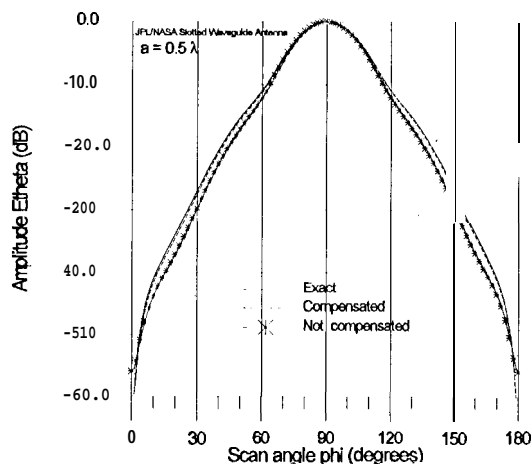


Figure 9. Comparison of exact solution and far-fields from simulated near-field with and without probe compensation.

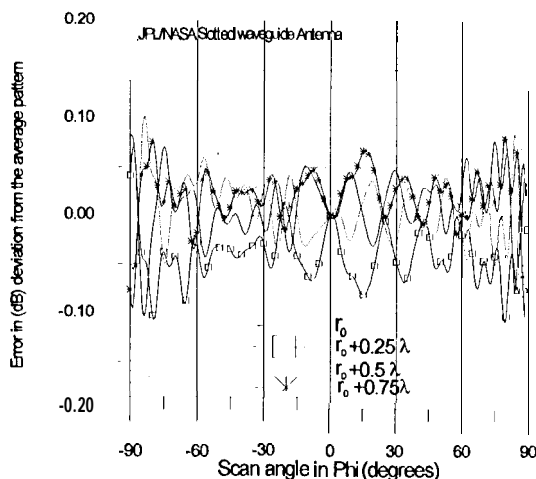


Figure 10. Error estimate on the far-field patterns due to NF multiple reflection between probe and AUT vs scan angle phi.

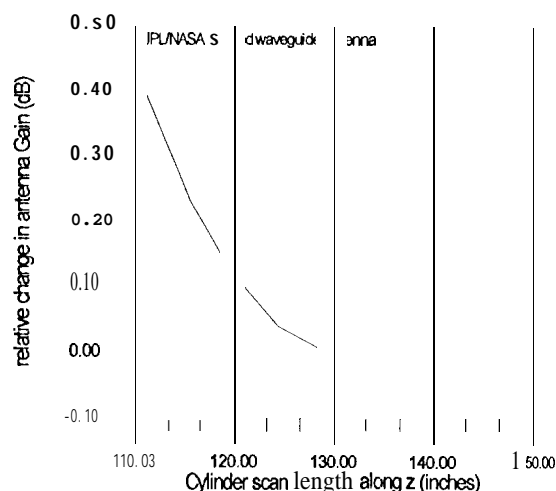


Figure 11. Relative change of antenna gain vs. truncated cylinder length in z-direction (AUT length 120.5in).

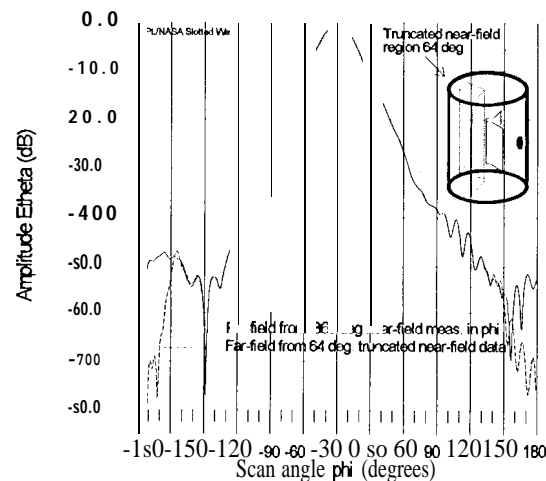


Figure 12. Comparison of far-field constructed from 360 deg near-field measurement in phi and 64 deg truncation in phi.

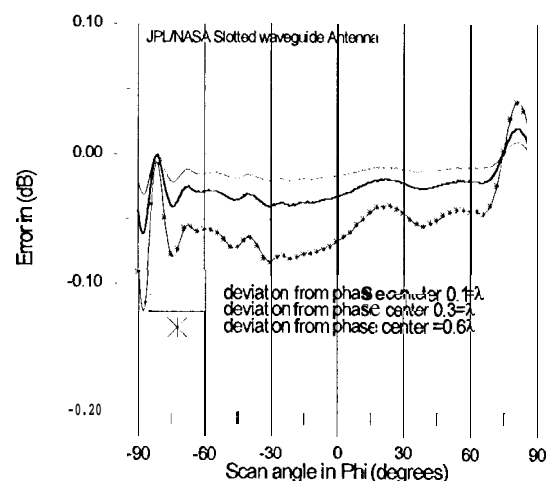


Figure 13. Error estimate on far-field patterns due to near-field radial distance measurement vs. scan angles in phi.